remote sensing

MDPI

Article

# The Spatio-Temporal Variability in the Radiative Forcing of Light-Absorbing Particles in Snow of 2003–2018 over the Northern Hemisphere from MODIS

**Jiecan Cui [1,2], Xiaoying Niu [1], Yang Chen [1], Yuxuan Xing [1], Shirui Yan [1], Jin Zhao [3], Lijun Chen [2], Shuaixi Xu [2], Dongyou Wu [1], Tenglong Shi [1], Xin Wang [1,4] and Wei Pu [1,]***

[1] Key Laboratory for Semi-Arid Climate Change of the Ministry of Education, College of Atmospheric Sciences, Lanzhou University, Lanzhou 730000, China
[2] Zhejiang Development & Planning Institute, Hangzhou 310030, China
[3] China Xi'an Satellite Control Center, Xi'an 710000, China
[4] Institute of Surface-Earth System Science, Tianjin University, Tianjin 300072, China
* Correspondence: puwei@lzu.edu.cn

**Abstract:** Light-absorbing particles (LAPs) deposited on snow can significantly reduce surface albedo and contribute to positive radiative forcing. This study firstly estimated and attributed the spatio-temporal variability in the radiative forcing (RF) of *LAPs* in snow over the northern hemisphere during the snow-covered period 2003–2018 by employing Moderate Resolution Imaging Spectroradiometer (MODIS) data, coupled with snow and atmospheric radiative transfer modelling. In general, the *RF* for the northern hemisphere shows a large spatial variability over the whole snow-covered areas and periods, with the highest value (12.7 W $m^{-2}$) in northeastern China (NEC) and the lowest (1.9 W $m^{-2}$) in Greenland (GRL). The concentration of *LAPs* in snow is the dominant contributor to spatial variability in *RF* in spring (~73%) while the joint spatial contributions of snow water equivalent (SWE) and solar irradiance (SI) are the most important (>50%) in winter. The average northern hemisphere *RF* gradually increases from 2.1 W $m^{-2}$ in December to 4.1 W $m^{-2}$ in May and the high-value area shifts gradually northwards from mid-altitude to high-latitude over the same period, which is primarily due to the seasonal variability of *SI* (~58%). More interestingly, our data reveal a significant decrease in *RF* over high-latitude Eurasia (HEUA) of −0.04 W $m^{-2}$ $a^{-1}$ and northeastern China (NEC) of −0.14 W $m^{-2}$ $a^{-1}$ from 2003 to 2018. By employing a sensitivity test, we find the concurrent decline in the concentration of *LAPs* in snow accounted for the primary responsibility for the decrease in *RF* over these two areas, which is further confirmed by in situ observations.

**Keywords:** light-absorbing particles (LAPs); remote sensing; snow albedo; radiative forcing

check for updates

**Citation:** Cui, J.; Niu, X.; Chen, Y.; Xing, Y.; Yan, S.; Zhao, J.; Chen, L.; Xu, S.; Wu, D.; Shi, T.; et al. The Spatio-Temporal Variability in the Radiative Forcing of Light-Absorbing Particles in Snow of 2003–2018 over the Northern Hemisphere from MODIS. *Remote Sens.* **2023**, *15*, 636. https://doi.org/10.3390/rs15030636

Academic Editor: Ralph R. Ferraro

Received: 28 November 2022
Revised: 12 January 2023
Accepted: 17 January 2023
Published: 21 January 2023

## 1. Introduction

Land surface albedo is defined as the ratio of solar radiation reflected by the land surface to total incident solar radiation and constitutes a key parameter in the regulation of Earth's energy budget [1]. For snow-covered regions at middle and high latitudes, albedo is one of the most potent positive feedback processes influencing the northern hemisphere climate [2]. Pure snow has the highest albedo of all natural surfaces and, as such, exerts a measurable cooling effect on regional climate [3]. Deposition of light-absorbing particles (LAPs), such as black carbon, dust, and organic carbon, could observably change the optical characters of snow [4–9], thereby contributing to positive radiative forcing via reduced albedo and enhanced absorption of incident solar irradiance [10–13]. Cui et al. (2021) [14] noted that, under all-sky conditions, a ~2% reduction occurred in albedo due to snowpack *LAPs* with ~3 W $m^{-2}$ radiative forcing over snow-covered portion for the northern hemisphere, which was approximately equivalent to doubling the concentration of atmospheric $CO_2$ [15].

Our understanding of radiative forcing (RF) by *LAPs* in snow is primarily based on a limited set of ground-based observations, model simulations, and remote sensing retrievals, and thus remains incomplete [16–18]. To date, several investigations have capitalised on the high accuracy of ground-based observations to explore *RF*. Of these, a previous study by Dang et al. (2017) [19] presented January–March *RF* in northern China (7–18 W $m^{-2}$), North America (0.6–1.9 W $m^{-2}$), and the Arctic (0.1–0.8 W $m^{-2}$), measured during a single year, and Ganey et al. (2017) [20] reported a daily averaged *RF* of 21.6 ± 5.9 W $m^{-2}$ for an Alaskan icefield during the 2014 ablation season. Other studies both presented 6-year (2005–2010) records of energy balance measurements for the Senator Beck Basin, Colorado, which showed that daily mean *RF* in springtime were 31–49 W $m^{-2}$ in the alpine zone and 45–75 W $m^{-2}$ in the sub-alpine zone [10,21]. Recognising the high-resolution of these in situ measurements, ground-based observations nonetheless remain poorly representative on regional and global scales owing to their inherently limited spatial coverage and temporal discontinuity [22–24].

Regional and global climate models have been used to capture the estimate of *RF* more comprehensively. In a study of the Arctic and northern China albedo, the Community Atmosphere Model (CAM5) was coupled with the Snow, Ice, and Aerosol Radiative (SNICAR) model to implement a sensitivity study of seasonal *RF* variability [25]. They reported that the *RF* in northern China was spatially variable, ranging from maximum values of 5–10 W $m^{-2}$ to <2 W $m^{-2}$ [25]. Meanwhile, Young et al. (2014) [26] combined the Fall3D and SNICAR models to simulate the *RF* from an eruption of Alaska's Redoubt Volcano and reported that mean daily *RF* adjacent to the vent attained values as high as 96 W $m^{-2}$. A more current study by Skiles et al. (2019) [27] coupled a multi-layer, physically based snow-process model (SNOWPACK) and the SNICAR model to simulate daily *RF* values of 30 W $m^{-2}$ in the snowmelt seasons at the Senator Beck Basin Study Area. However, non-negligible uncertainties still exist although the numerical models play a huge part in the understanding of LAP causing climate forcing [27].

Remote sensing affords a refined approach to balancing accuracy and spatio-temporal representation when evaluating real-time *RF*, thereby helping narrow the gap between our understanding of snowpack *LAPs* and estimates of their global radiative impact [28,29]. For instance, Bryant et al. (2013) [30] employed data retrieved from the NASA Moderate Resolution Imaging Spectroradiometer (MODIS) to estimate ablation season *RF* in the southern Colorado Rockies during the period 2000–2010, and they reported an interannual range of 20–80 W $m^{-2}$. In the European Alps, the instantaneous *RF* values were reported in 2014 of up to 153 W $m^{-2}$, using Landsat 8 Operational Land Imager (OLI) datasets coupled with optical sensor output from an Unmanned Aerial Vehicle (UAV) [31]. Elsewhere, Chen et al. (2021) [32] employed MODIS data to retrieve wintertime *RF* values for northwestern China (Xinjiang) during the period 2001–2018, during which the regional mean value was 20.43 ± 7.3 W $m^{-2}$. It should be noted that most prior remote-sensing-based studies have focused on specific locations, limited periods, and/or specific contributory factors. In contrast, the characters and drivers of long-term *RF* variability have received far less attention; as a result, our understanding of *RF* remains fundamentally incomplete. Thus, to strengthen research into regional- and global-scale climatic and hydrologic change, a systematic evaluation of longer-term seasonal and interannual *RF* is warranted [33]. Compared with the spatial and seasonal patterns, understanding the long-term changes of northern hemisphere *RF* over the last several decades is also arguably of greater importance to the scientific community due to its sensitivity to climate change and its key role in global climate and hydrology [2,34]. To date, however, little attention has been focused on long-term variability due to the inherent limitations of existing methods. Although previous field campaigns have compiled a large number of snow samples and provided extensive *LAPs* content data for the northern hemisphere snowpack, long-term measurements of *LAPs* in seasonal snow at stationary sites remain rare [10,33,35–37] and cannot reflect regional- and global-scale variance effectively. For instance, whereas ice cores afford long-term, high-resolution datasets, they are geographically restricted to specific areas, such as the

Arctic, Antarctic, and High Mountain Asia [38,39]; extensive tracts subject to seasonal snow are thus poorly represented. Conversely, numerical climate models are subject to parameter uncertainties and biases inherited from emission inventories, resulting in considerable simulation uncertainty [40,41]. For instance, although the CMIP6 emission inventory (developed in partnership with the Community Emissions Data System) has improved existing inventories, made the methodology more consistent and reproducible, this dataset nonetheless overestimates Asian emissions of anthropogenic-source *LAPs* (e.g., black carbon and organic carbon) over the last decade (IPCC6 AR6, 2021).

To better investigate the long-time sequenced *RF* variability across the northern hemisphere over the snow-covered period, we sought to answer two questions: First, how do the spatial characteristics of northern hemisphere *RF* vary on monthly scales, and which factors are primarily responsible for this variability? Second, are temporal variations in *RF* significant on both seasonal and interannual scales, and if so, what are the dominant factors driving such temporal variability in different regions? We employ satellite data coupled with radiative transfer modelling to retrieve *RF* values for the northern hemisphere, after which we quantitatively calculate the contributions of various physical factors to *RF* variations. This paper is organised as follows. A short summary of all the materials and methodology utilised is in Section 2. Section 3.1 represents the December–May monthly averaged *RF* across the northern hemisphere during the period 2003–2018. Section 3.2 analyses the impacts of different factors on spatial variations in *RF*. Section 3.3 gives the seasonal variations of *RF* as well as qualitative and quantitative analysis of the relationships between *RF* and influencing factors. Section 3.4 analyses the variations of *RF* at an interannual scale and discusses the significant decrease in regional *RF* and the contributions of different factors to this decrease. Sections 4 and 5 cover the discussion and conclusions.

## 2. Materials and Methods

### 2.1. MODIS Datasets

To retrieve *RF*, we use MODIS collection 6 products obtained from the National Aeronautics and Space Administration (NASA (Washington, DC, USA): https://earthdata.nasa.gov/ (accessed on 15 October 2022)). Specifically, the MCD43 series dataset is a widely used and rigorously validated surface albedo product that provides local noontime solar zenith angles and percentage cell snow cover. For this study, we utilise 0.05° spatial resolution (climatic cell grid), daily composite MCD43C3 data (weighted to the 9th day of every 16-day observation cycle), which comprises both Aqua and Terra measurements, collected between December and May over the period 2003–2018. Daily albedo is inversed through the Bidirectional Reflectance Distribution Function (BRDF) and albedo parameter product [42,43] for daily cloud-free grid cells. Initial MODIS BRDF observations are subsequently inversed to provide black-sky and white-sky albedo values, calculated at local solar noon.

Black-sky albedo is the directional hemispherical reflectance (DHR) and is defined as a function of the solar zenith angle under conditions of zero diffuse solar radiation. In contrast, white-sky albedo is the bi-hemispherical reflectance (BHR) under isotropic illumination without direct beam solar radiation; this parameter is thus independent of the solar zenith angle. The albedo is strictly quality controlled, therefore, by the quality of the BRDF. Here, we use cells for which the BRDF quality flag is $\leq 4$ when the noontime zenith angle is $<80°$, such that cells with $>50\%$ fill values, which are without full BRDF inversions due to non-functional or noisy detectors, are eliminated [44]. Although insufficient observations can mean that albedo is not effectively derived from BRDF inversions, the magnitude of inversions is processed through a prior empirical algorithm which performed well under most scenes [45,46], and the uncertainty of these albedo data is mostly less than 5% [47]. Annual land cover type is derived from MCD12C1 (0.05° spatial resolution), which is served to minimise the impact of the forest canopy to accurately access land surface albedo.

### *2.2. CERES Datasets*

The Clouds and the Earth's Radiant Energy System (CERES) project estimates radiation budgets at the land surface and the top of atmosphere (TOA) at 1° spatial resolution. We employ the SYN1deg products (which provide surface daily averaged downward shortwave solar radiation fluxes and fractions of cloud cover) to calculate *RF* values under all-sky conditions. SYN1deg combines both Terra and Aqua observations and includes initial, hourly geostationary measurements of narrowband radiance, which are then calibrated via MODIS to maintain consistency [48].

### *2.3. ERA5 Snow Water Equivalent Data*

ERA5 re-analysis datasets are the current generation products provided by the European Centre for Medium-Range Weather Forecasts (ECMWF; Hersbach et al., 2020 [49]) and exhibit greatly improved spatial resolution and performance over its predecessors. This is particularly true for the estimation of liquid water in snow, the snow cover fraction derivation equation, and the evolution of snow density [50–53]. For our study, we use the ERA5 snow water equivalent (SWE) product at 0.25° spatial resolution and hourly interval. The data are processed with the Interactive Multisensor Snow and Ice Mapping System (IMS), which provides gridded snow depth as well as snow cover fractions using in situ station observations [54].

### *2.4. Radiation Transfer Models*

The Santa Barbara DISORT Atmospheric Radiative Transfer (SBDART) model was developed in 1998 by the University of California, specifically for analysing radiative transfer issues of satellite-borne remote sensing and atmospheric radiation balance data. Incorporating standard atmospheric models, underlying surface models, and cloud models along with latitude-specific vertical-distribution models for aerosols, the SBDART model could calculate direct and diffuse radiation in the form of surface downward shortwave fluxes under both clear and cloudy conditions.

Based on the two-stream theory [55] and incorporating snowpack *LAPs*, the Snow, Ice, and Aerosol Radiative (SNICAR) model developed by Flanner et al. (2007) [56] is a multi-layer heterogenous radiative transfer schema used to calculate snow albedo. SNICAR has been applied extensively in Earth System Models and is a reliable tool for simulating snow albedo accurately [57,58]. In their recent study, Dang et al. (2019) [59] modified SNICAR by incorporating the delta-Eddington Adding-Doubling [60] scheme, which repeatedly calculated the transmittance, reflectance, and refractive boundary for individual snow layers before combining all layers to calculate the optical characteristics for the snow column totally. In superseding the methodology by Toon et al. (1989) [55], this approach achieves higher overall accuracy. In our study, we use the newest version of SNICAR (SNICAR-Adv3) to compute snow albedo under multiple incident radiation and snow water equivalent conditions, effective snow grain sizes, solar zenith angles, and LAP contents [61]. In this study, we assume the spherical snow grain shape and external mixing of LAPs-snow with one-layer snowpack when combining the remote sensing snow products derived from MODIS and simulated results by SNICAR as in previous studies [56,62]. For each calculation, we assume clear-sky conditions for direct incident radiation (black sky) and cloudy conditions for the diffuse component of irradiance (white sky) with a continuous 300–2500 nm downward solar spectrum of a 10 nm interval in SNICAR to refer to broadband albedo.

### *2.5. Radiative Forcing Retrievals*

The deposition of *LAPs* in snow principally reduces the snow albedo in the ultraviolet as well as visible wavelengths and has little influence on near-infrared (NIR) wavelengths. By comparison, snow grain sizes (*SGS*) and solar zenith angle (*SZA*) affect the snow albedo basically in NIR wavelengths. Definitely, snow albedo reduces as *SGS* increases and *SZA* decreases [4,5,14]. The snow albedo is quantitatively retrieved from MODIS data along with radiative transfer models in this study.

### 2.5.1. Retrievals of Blue-Sky Albedo from MODIS

For both clear-sky and cloudy conditions, we utilize SBDART to compute direct and diffuse spectral incident radiation with a 10 nm interval, level-surface noontime values for a range of latitudes at 1° intervals. We then correct the plane-radiation to terrain-radiation in conjunction with the local slope and aspect, obtained through the Shuttle Radar Topography Mission (SRTM) digital elevation model, which is according to the terrain correction algorithm as follows [63]:

$$\cos\beta = \cos\theta_0\cos\theta_T + \sin\theta_0\sin\theta_T\cos(\phi_0 - \phi_T) \tag{1}$$

where $\theta_0$ refers to the solar zenith angle for a horizontal surface; $\phi_0$ denotes the solar azimuth angle ($\phi_0 = \pi/2$ at local noon); $\theta_T$ and $\phi_T$ are slope inclination and aspect, respectively; and $\beta$ indicates the local solar zenith angle.

MCD43 includes albedo at local noontime in different conditions (black-sky and white-sky albedo). SNICAR also simulates snow albedo under two radiation scenarios (direct and diffuse). The actual albedo at wavelength $\lambda$ (also known as blue-sky albedo: $\alpha_{MODIS,\lambda}^{blue-clear}$) under clear-sky conditions can be presented:

$$\alpha_{MODIS,\lambda}^{blue-clear} = f_{dif,\lambda}^{clear}\cdot\alpha_{MODIS,\lambda}^{white-sky} + \left(1 - f_{dif,\lambda}^{clear}\right)\cdot\alpha_{MODIS,\lambda}^{black-sky} \tag{2}$$

where $\alpha_{MODIS,\lambda}^{white-sky}$ and $\alpha_{MODIS,\lambda}^{black-sky}$ are white-sky and black-sky albedo from MODIS. $f_{dif,\lambda}^{clear}$ represents the proportion of diffuse components in the total solar irradiance under clear-sky conditions and can be calculated as follows [64]:

$$f_{dif,\lambda}^{clear} = \frac{E_{dif}^{clear}(\lambda;\ \varphi)}{E_{dif}^{clear}(\lambda;\ \varphi) + E_{dir}^{clear}(\lambda;\ \varphi)\cdot\cos\beta} \tag{3}$$

where $\varphi$ refers to latitude, $E_{dif}^{clear}(\lambda;\ \varphi)$ and $E_{dir}^{clear}(\lambda;\ \varphi)$ are the diffuse and direct components of solar irradiance calculated by SBDART, respectively, under clear-sky conditions. The blue-sky albedo under cloudy-sky conditions ($\alpha_{MODIS,\lambda}^{blue-cloudy}$) can be calculated analogously. Subsequently, the CERES cloud fraction ($CF$) is used to calculate blue-sky albedo under all-sky conditions ($\alpha_{MODIS,\lambda}^{blue-all}$):

$$\alpha_{MODIS,\lambda}^{blue-all} = CF\cdot\alpha_{MODIS,\lambda}^{blue-cloudy} + (1 - CF)\cdot\alpha_{MODIS,\lambda}^{blue-clear} \tag{4}$$

### 2.5.2. Identification of Snow-Covered Area and Retrievals of Snow Albedo

The identified snow-covered area (ISCA) requests the Normalized Difference Snow Index ($NDSI$) and snow albedo at band 4 ($\alpha_{MODIS,\lambda=555\ nm}^{blue-all}$) are greater than 0.6 [63]. The empirical formula between Fractional Snow Cover ($FSC$) and $NDSI$ is as follows:

$$FSC = -0.01 + 1.45\cdot NDSI \tag{5}$$

It should be noted that the $FSC$ of ISCA is >86% when $NDSI > 0.6$, which results in the $FSC$ not necessarily 100%. Hence, the snow albedo ($\alpha_{snow,\lambda}^{blue-all}$) needs to be separated from the mixed pixels, which is not covered completely by snow:

$$\alpha_{MODIS,\lambda}^{blue-all} = FSC\cdot\alpha_{snow,\lambda}^{blue-all} + (1 - FSC)\cdot\alpha_{underlying,\ \lambda} \tag{6}$$

where $\alpha_{underlying,\ \lambda}$ is the albedo of other underlying surface types [65].

### 2.5.3. Retrievals of Snow Grain Sizes

The snow grain sizes (*SGS*) are retrieved at a wavelength of ~1240 nm (MODIS band 5) by fitting the snow albedo simulated and retrieved from SNICAR and MODIS, respectively, according to the method of Nolin and Dozier (2000) [66], which algorithm is not affected by water vapour or liquid water and has been extensively applied in previous studies [67,68]. This method exactly has uncertainty (less than 20%) in retrieving snow grain size [58,69], which is an economical and practical tool to perform quick access to hemisphere-scale assessment of the properties of the snowpack.

### 2.5.4. Retrieval of *RF*

The snow albedo retrieved from MODIS ($\alpha^{blue-all}_{MODIS,\lambda}$) is fitted to a continuous spectrum (300–2500 nm with a 10 nm resolution) according to the methodology from Cui et al. (2021) [14]. Then, the broadband snow albedo reduction caused by *LAPs* ($\Delta\alpha^{LAPs}_{MODIS,\ noon}$) is calculated under all-sky conditions at local noon time, multiplying the deviation between pure snow albedo simulated from SNICAR ($\alpha^{blue-all}_{pure,\lambda}$) and snow albedo retrieved from MODIS ($\alpha^{blue-all}_{MODIS,\lambda}$) by solar irradiance:

$$\Delta\alpha^{blue-all}_{broadband} = \frac{\int_{300\ nm}^{2500\ nnm}\left(\alpha^{blue-all}_{pure,\lambda} - \alpha^{blue-all}_{MODIS,\lambda}\right)\cdot E_{all,\lambda}\cdot d\lambda}{\int_{300\ nm}^{2500\ nm} E_{all,\lambda}\cdot d\lambda} \tag{7}$$

$$RF_{daily} = \Delta\alpha^{blue-all}_{broadband}\cdot SW_{all} \tag{8}$$

where $SW_{all}$ denotes the daily mean downward solar fluxes (shortwave) under all-sky conditions via CERES.

## *2.6. Attribution of Spatio-Temporal Variability in Radiative Forcing*

As previous studies (e.g., Wu et al., 2021 [70]; Cui et al., 2021 [14]; Jin et al., 2022 [71]), *RF* is dependent primarily on the concentration of *LAPs*, snow grain size (*SGS*), snow water equivalent (*SWE*), solar zenith angle (*SZA*), cloud fraction (*CF*), and solar irradiance (*SI*). An impurity index ($I_{imp}$) is utilised to represent the LAP concentration in snow [31,58]:

$$I_{imp} = \frac{\ln\left(\alpha^{blue-all}_{MODIS,band4}\right)}{\ln\left(\alpha^{blue-all}_{MODIS,band5}\right)} \tag{9}$$

where $\alpha^{blue-all}_{MODIS,band4}$ and $\alpha^{blue-all}_{MODIS,band5}$ are the snow albedo retrieved from MODIS at wavelengths of 555 nm (band 4) and 1240 nm (band 5), respectively. The $RF_{daily}$ could be calculated as follows:

$$RF_{daily} = f(LAPs, SGS,\ SWE,\ SZA,\ CF,\ SI) \tag{10}$$

The spatial variability in *RF* due to *LAPs* can be expressed as

$$RF_{daily}(LAPs) = f\left(LAPs, \overline{SGS},\ \overline{SWE},\ \overline{SZA},\ \overline{CF},\ \overline{SI}\right) \tag{11}$$

where $\overline{SGS}$, $\overline{SWE}$, $\overline{SZA}$, $\overline{CF}$, $\overline{SI}$ denote spatially averaged values of *SGS*, *SWE*, *SZA*, *CF*, and *SI*. We quantify the spatial variability due to other factors $(RF_{daily}(X_i))$ in a similar manner, after which we apply multiple linear regression to fit *RF*:

$$RF^{fit}_{daily} = \sum\nolimits_1^n a_i\cdot RF_{daily}(X_i) \tag{12}$$

where $RF_{daily}^{fit}$ is the fitted *RF*, $a_i$ denotes the regression coefficients, $X_i$ represents the various factors driving variability in *RF*, and $n$ is the number of those driving factors. The attribution of the spatial variance in *RF* can therefore be expressed as follows:

$$RF_{daily}^{fit} - \overline{RF_{daily}^{fit}} = \sum\nolimits_1^N a_i \cdot \left(RF_{daily}(X_i) - \overline{RF_{daily}(X_i)}\right) \tag{13}$$

in which $RF_{daily}^{fit} - \overline{RF_{daily}^{fit}}$ is the *RF* anomaly ($RF_{daily,\ anomaly}^{fit}$). Equation (13) can be written as:

$$RF_{daily,\ anomaly}^{fit} = \sum_1^N a_i \cdot RF_{daily,\ anomaly}(X_i) \tag{14}$$

According to Huang and Yi (1991) [72] and Cui et al. (2021) [14], the fractional contribution of factors to the spatial variability in *RF* ($FC_{RF}^{X_i}$) can be calculated as:

$$FC_{RF}^{X_i} = \frac{1}{m} \sum_{j=1}^{m} \frac{\left(a_i \cdot RF_{daily,anomaly}(X_i)_j\right)^2}{\sum_{i=1}^{6} \left(a_i \cdot R_{daily,anomaly}(X_i)_j\right)^2} \tag{15}$$

in which $m$ denotes the length of the data set. Similarly, we obtain the fractional contribution of factors to temporal *RF* variability by calculating the spatial-mean $\overline{X_i}$ for monthly and multi-year averages.

### 2.7. Sensitivity of Interannual Variation of RF

Sensitivity tests are conducted to assess the impact of different factors on the interannual variation of *RF* from 2003 to 2018 referring to the similar method of Räisänen et al. (2017) [73]. The sensitivity diagnosis of certain factors is through recalculating *RF* using Equations (1)–(8) while other factors are fixed as multi-year mean averages. We recalculate six experiments to isolate the single effects of each factor. Then the Mann–Kendall (MK) test, which is a non-parametric test to identify the significance of the trend in time series data, is applied to analyze the trend in *RF* caused by different factors. These tests enable us to quantify the absolute *RF* sensitivity caused by different factors (W $m^{-2}$ per year). The sensitivity estimate (regression slope), which is a result of *RF* variability and the strength of the relationship of the driving factors, would be helpful for us to understand the interannual variability of *RF*.

## 3. Results

### 3.1. Spatial Distributions of RF in the Northern Hemisphere

Focusing on the 2003–2018 identified snow-covered area (ISCA), Figure 1 shows the spatial distributions of average radiative forcing due to snowpack *LAPs* between December and May. ISCA is distributed widely throughout the northern hemisphere and can be separated into six broad regions according to geographical distribution and *RF* magnitude. These regions include high-latitude North America (HNA), Greenland (GRL), high-latitude Eurasia (HEUA), mid-latitude North America (MNA), mid-latitude Eurasia (MEUA), and northeastern China (NEC). We note that there are no data for much of some regions, such as Russia, Canada and Europe, which are covered by forests (Figure S1), as snow radiation cannot transparent the canopy, although these areas are represented covered by snow. So, the *RF* statistics are calculated only for the ISCA and our study period, consistent with prior research [14]. In general, the average *RF* for the northern hemisphere over the snow-covered period is 3.4 W $m^{-2}$, with the highest value (12.7 W $m^{-2}$) observed in NEC and the lowest (1.9 W $m^{-2}$) in GRL. For HNA, HEUA, MNA, and MEUA, the *RF* values are 3.2, 3.1, 3.6, and 3.1 W $m^{-2}$, respectively, which are comparable to the northern hemisphere average and consistent with field-based measurements [19,74–78]. The spatial patterns depicted in Figure 1 also align with the simulated model output [25,40,56,79–81].

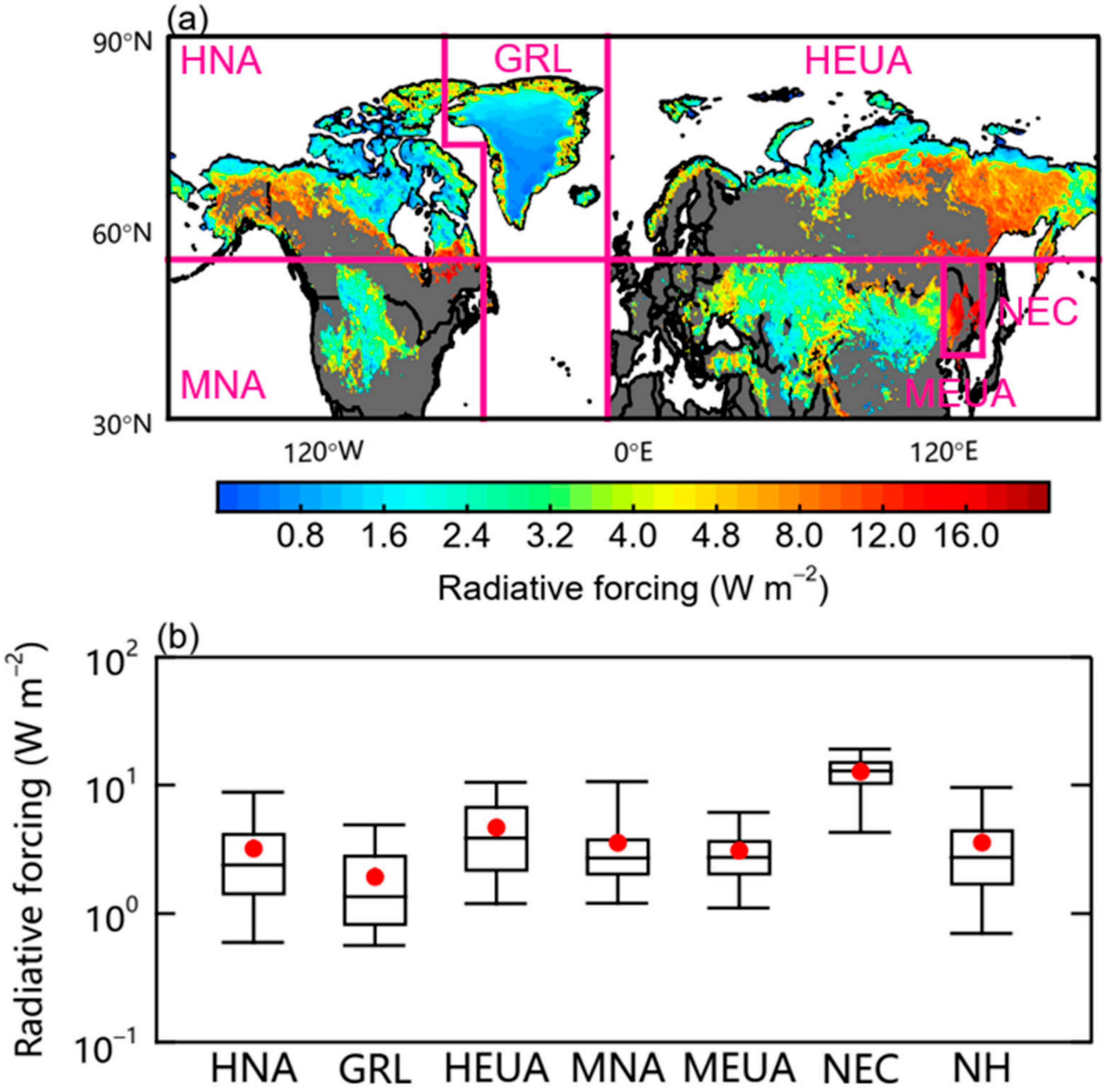

**Figure 1.** Spatial distributions of average December–May (**a**) radiative forcing for the period 2003–2018 and (**b**) statistics for regionally averaged radiative forcing for the northern hemisphere ISCA. Boxes are the 25th and 75th quantiles; horizontal lines represent the 50th quantiles (medians). Red dots denote averages, and whiskers represent the 5th and 95th quantiles.

Between winter and spring, the spatial coverage of ISCA varies from month to month. For instance, during December and January (Figure 2a,b), ISCA extends primarily over mid-latitude regions (MNA, MEUA, and NEC) but is absent from high latitudes (HNA, GRL, and HEUA), where the polar night precludes satellite-based detection of snow cover and renders *RF* negligible [14]. Between those two months, the spatial patterns of northern hemisphere *RF* are broadly similar, with January values being somewhat higher than those for December. Regionally, *RF* values are highest in NEC, followed by MNA and MEUA. In February, as the mid-latitude snow cover begins to shrink (Figure 2c), *RF* values continue to rise in NEC, MNA, and MEUA owing to increased solar radiation. Furthermore, values in the margins of MNA, MEUA, and NEC are routinely higher than those for internal regions; we attribute this pattern to the thinner, less continuous snow cover in marginal areas, which results in greater exposure of soil and vegetation and thus incorporation of wind-blown soil particles and plant debris [28]. Enhanced transport of anthropogenic pollution from adjacent snow-free areas may also be a contributing factor [78]. In contrast to the middle latitudes, ISCA retrieval at high latitudes commences at the end of the polar night and the onset of solar irradiation. Average *RF* values for HNA and HEUA are broadly similar, and both are higher than the values for GRL.

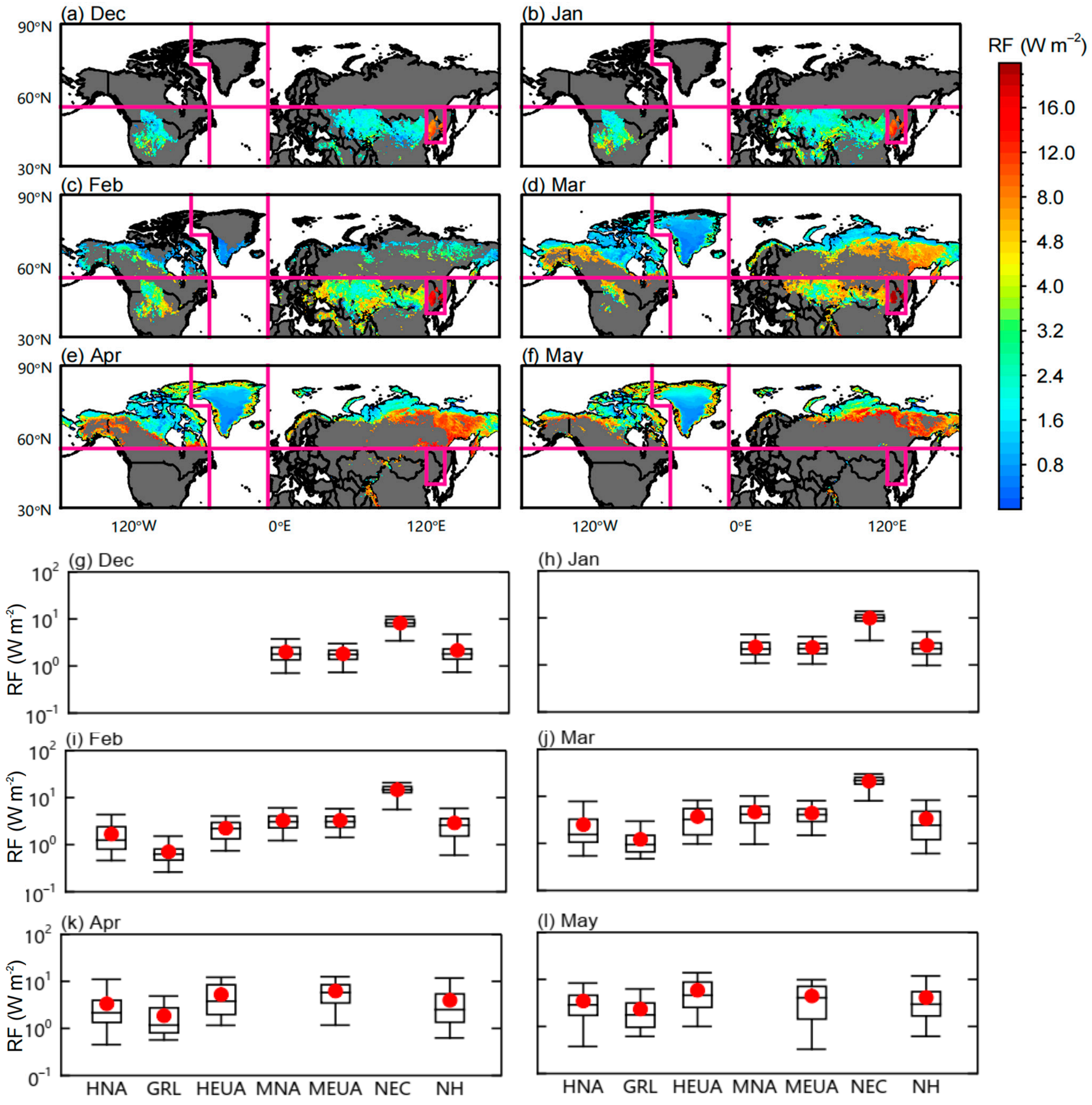

**Figure 2.** Spatial distributions of averaged December–May (**a**–**f**) radiative forcing for the period 2003–2018 and (**g**–**l**) statistics for regionally averaged *RF* for the northern hemisphere ISCA. Boxes are the 25th and 75th quantiles; horizontal lines represent the 50th quantiles (medians). Red dots denote averages, and whiskers represent the 5th and 95th quantiles.

In March, as the mid-latitude snowpack continues to melt, *RF* attains peak values in NEC and MNA. At higher latitudes, where the entire snow-covered area is now retrievable, the ISCA reaches its maximum extent of the six-month observation period. In GRL, *RF* values are uniformly higher over coastal regions than inland areas, in agreement with field measurements [82]. In HNA, MEUA, and HEUA, *RF* exhibits a decreasing trend with latitude that reflects the spatial variability of solar radiation. By April, NEC and MNA are almost entirely free of seasonal snow, with only a few remnants remaining in high-elevation and/or mountainous regions of MEUA (e.g., the Tibetan Plateau). Maximum *RF* values occur in these mountainous areas because of the relatively strong solar irradiance at high elevations, followed by HEUA, HNA, and GRL. By May, the *RF* in HEUA has exceeded that of MEUA, and the longer daylight hours at higher latitudes means that *RF* values would be higher in northern interior GRL than that over southern parts of the island.

### 3.2. Attribution of Spatial Variability in RF

To explore the spatial characteristics and evolution of northern hemisphere *RF* in greater detail, we employ the snow impurity index ($I_{imp}$, an indicator of snowpack LAP content; Di Mauro et al., 2015 [31]) along with parameters *SGS*, *SZA*, *SWE*, *SI*, and *CF* (Figure 3), which together determine the changes in *RF* (see Section 2.6). Generally, $I_{imp}$ exhibits a strong spatial inhomogeneity throughout the northern hemisphere during December–May (Figure 3a), with maximum values in NEC, HEUA, and the margins of HNA. This pattern aligns with the distribution of high *RF* values. Furthermore, the scatterplots given in Figure 4a reveal a strong positive correlation between *LAPs* and *RF* (correlation coefficient > 0.6), demonstrating the importance of $I_{imp}$ in the spatial distribution of *RF*. Similarly, *SGS* exhibits a heterogenous spatial distribution and significant correlation coefficient with *RF* (Figures 3b and 4b), whereas *SWE* generally increases with latitude and thus is negatively correlated with *RF*. Although the spatial distributions of *SZA* and *SI* are both largely latitude dependent, we note that the former is positively correlated with *RF* and the latter negatively correlated. In contrast, *CF* exhibits a complex distribution, with a generally negative impact on *RF*.

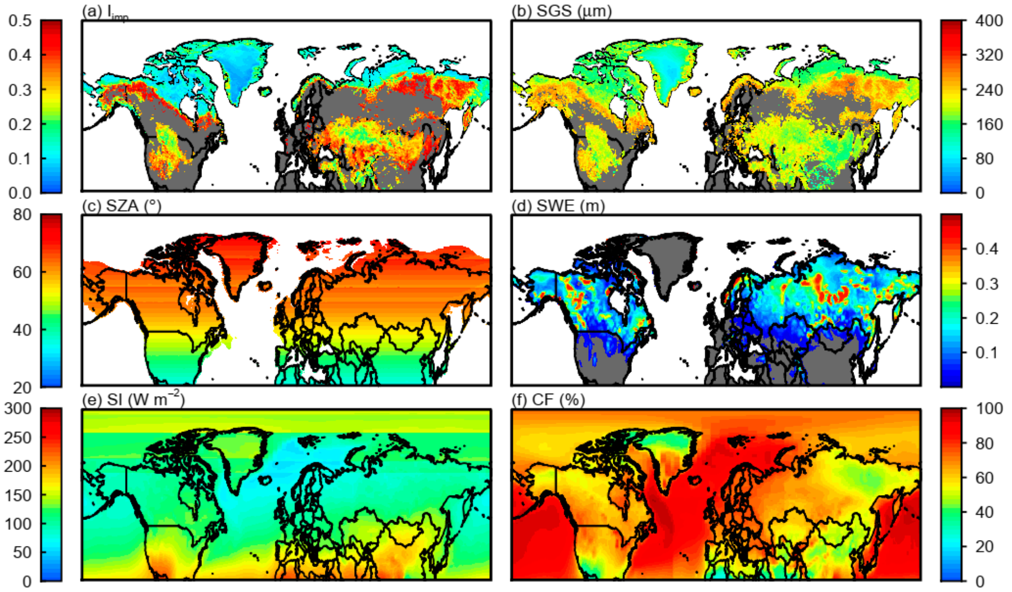

**Figure 3.** Spatial distributions of December–May averaged (**a**) $I_{imp}$ (retrieved from MODIS), (**b**) *SGS* (retrieved from MODIS), (**c**) *SZA* (MODIS), (**d**) *SWE* (ERA5), (**e**) *SI* (CERES), and (**f**) *CF* (CERES) for the period 2003–2018.

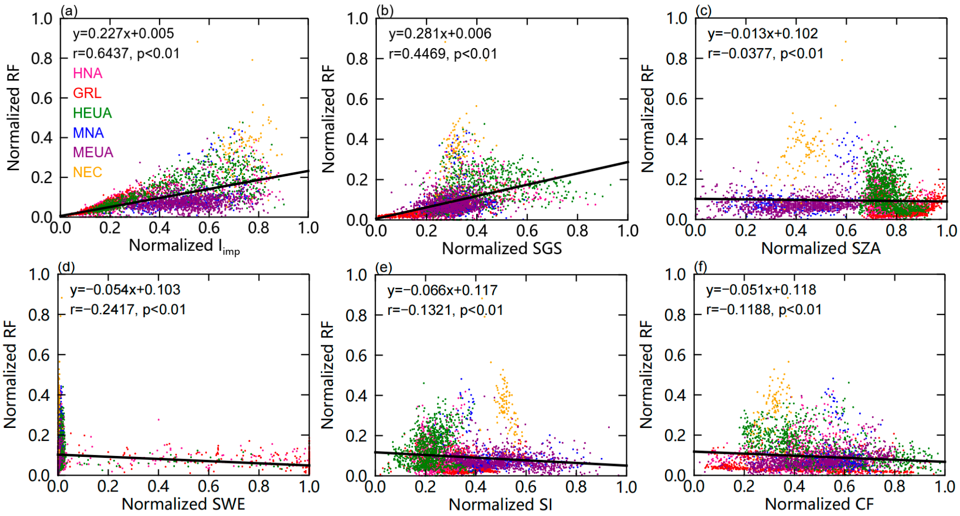

**Figure 4.** Scatterplots of normalized radiative forcing (RF) versus *RF*-dependent parameters. Panels (**a**–**f**) represent the scattering of $I_{imp}$, *SGS*, *SZA*, *SWE*, *SI*, and *CF*, respectively.

Augmenting the correlation analysis described above, we also sought to quantify the fractional contributions of every influencing factor to the spatial variability of *RF* (Figure 5) via the approach outlined in Section 2.6. For the northern hemisphere as a whole, the contributions of *SWE* and *SI* are greatest between December and February, whereas *LAPs* represent the dominant contributor (~60–85%) to springtime (March–May) *RF* spatial variability. This pattern reflects the fact that the wintertime ISCA is distributed primarily over middle latitudes, where *LAPs* exhibit minor spatial differences, whereas the springtime ISCA is broadly distributed over both middle (high $I_{imp}$ values) and high (low $I_{imp}$ values) latitudes, resulting in greater spatial variance in LAP contents (Figure S2).

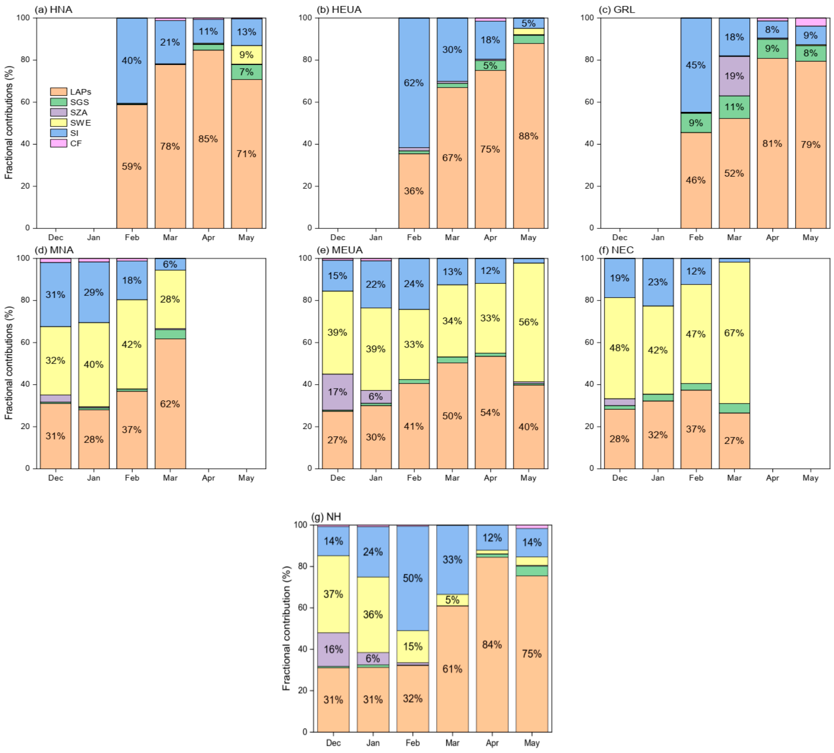

**Figure 5.** Fractional contributions of *LAPs*, *SGS*, *SZA*, *SWE*, *CF*, and *SI* to the spatial variability of radiative forcing. Panels (**a**–**f**) represent the regions HNA, GRL, HEUA, MNA, MEUA, and NEC, respectively; panel (**g**) represents the northern hemisphere as a whole.

Theoretical modelling [56] and laboratory experimentation [83] confirm that *RF* is more sensitive to changes in LAP content than to other influencing factors. In our study, neither *SWE* nor *SI* exhibit an obvious change in spatial distribution between December and May (Figures S5 and S6). Consequently, the largest contributor shifts from *SWE* and *SI* in winter to LAP content in spring. *LAPs* also play a dominant springtime role on a regional scale, with average contributions of >75% at high latitudes (HNA, HEUA, and GRL) and 55% at middle latitudes (MNA and MEUA; Figure 5a–e). In winter, the greatest contributor at high latitudes is *SI*, whereas *SWE* dominates the middle latitudes. One possible explanation for this pattern is that mid-latitude *SWE* is innately variable spatially and also relatively thin (Figure S5), thereby precluding a semi-infinite thickness at infrared and visible wavelengths [84] and impacting *RF* [78]. In contrast, the high-latitude snowpack is typically semi-infinite, such that *RF* is influenced by latitude-dependent *SI* but independent of *SWE*. One exception to this pattern is NEC, where *SWE* is routinely the greatest contributor to winter–spring *RF* spatial variability (Figure 5f), followed by *LAPs* and *SI*. This result reflects the combined influence of generally elevated LAP content [77], limited *SI* variability, and considerable *SWE* variance in NEC (Figure S5). Finally, the respective contributions of *CF*, *SZA*, and *SGS* to spatial *RF* variability are low for different regions and/or months.

The results described above differ from our correlation analysis output, for which *SZA* and *SGS* are significantly correlated with *RF*. We posit that this disparity is primarily due to the non-linear characteristics of snow radiative transfer, such that *RF* is more sensitive to the wide range of *SWE* values applied here than to *SZA* and *SGS*, which is in agreement with prior modelling results [58]. From a seasonal perspective, the LAP contribution increases from winter to spring both on global and regional scales, reaching peak values in April over most regions. In contrast, the *SI* contribution in HNA, HEUA, GRL, and MNA declines over time. We note that although *SWE* plays an important role in NEC, MNA, and MEUA during both winter and spring, its contribution to northern hemisphere *RF* is non-negligible only during winter.

In summary, *LAPs* are the largest contributor to spatial variability in springtime *RF* both on global and regional scales, with the notable exception of NEC. During winter, *SWE* and *SI* play dominant roles at middle and high latitudes, respectively, whereas the specific contributions of *CF*, *SZA*, and *SGS* are comparatively low.

### 3.3. Seasonal Variability and Attribution in RF

Figure 6a shows monthly variations in *RF* during 2003–2018, both for the six study regions and the whole northern hemisphere. On a hemispheric scale, *RF* exhibits a moderate increase from 2.1 W $m^{-2}$ in December to 4.1 W $m^{-2}$ in May; this clear seasonal pattern is a salient feature of most years between 2003 and 2018 (Figure S8). According to the snow radiative transfer mechanism [56], the observed decrease in *LAPs* and *SGS*, coupled with rising *SWE* and *CF*, could account for the decrease in *RF*, whereas increasing *SI* and declining *SZA* would tend to enhance radiative forcing. As a consequence, the synthesis effects drive an increase in *RF* over time, confirming that the overwhelmingly positive impact of *SI* and *SZA* on monthly *RF* variability is greater than the combined negative influence of *LAPs*, *SGS*, *CF*, and *SWE*.

At high latitudes, we observe similar patterns of seasonal *RF* variability in HNA, GRL, and HEUA, with May values being two times higher than February values. In addition, the majority of influencing factors (e.g., $I_{imp}$, *SGS*, *SI*, and *SZA*) at high latitudes reveal comparable degrees of seasonal variance to the northern hemisphere as a whole, suggesting that the combined positive impact of *SI* and *SZA* is responsible for rising *RF* between winter and spring. At middle latitudes, the pattern of seasonal variability is more spatially diverse. In MEUA, for example, *RF* increases between December and April but decreases again in May; in MNA, a gradual increase between December and March is followed by a strong increase in May; and in NEC, *RF* follows a persistently strong rising trend throughout the winter–spring period, with March values being more than two times higher than December values.

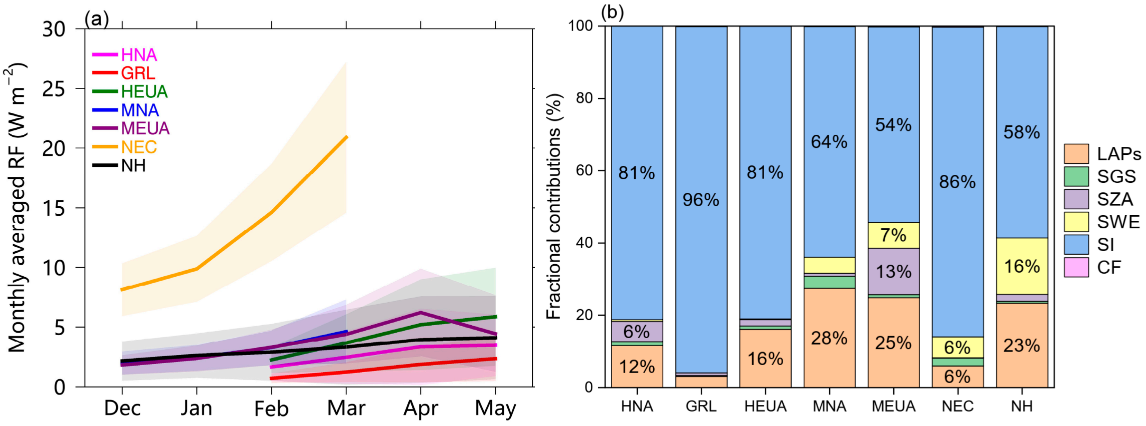

**Figure 6.** (**a**) Multi-year (2003–2018) monthly averaged radiative forcing (RF) variability for different regions. (**b**) Fractional contributions of *LAPs*, *SGS*, *SZA*, *SWE*, *SI*, and *CF* to the seasonal radiative forcing variability.

Recognising that the regional differences in seasonal *RF* variability reflect the combined impact of *LAPs*, *SGS*, *SZA*, *SWE*, *CF*, and *SI*, we sought to quantify the fractional contributions of each influencing factor using the methodology introduced in Section 2.6. As presented in Figure 6b, *SI* constitutes the dominant contributor in all six regions and the northern hemisphere generally, accounting for ~50–95% of seasonal variability. The contribution of *SI* is greater at high latitudes than at middle latitudes. In contrast, *LAPs* play a secondary role (contributing ~5–30%) and their impact appears to be more important at middle latitudes than at high latitudes. We note that these findings differ from the results of our spatial attribution analysis, in which *LAPs* are the dominant factor, suggesting that the drivers of *RF* variance differ between temporal and spatial perspectives. This possibility has not been evaluated in detail and should be prioritised in future research. Consistent with its role in spatial *RF* variability, *SWE* also contributes to mid-latitude and northern hemisphere scales. In contrast, the respective impacts of *SGS*, *SZA*, and *CF* are relatively low.

Overall, *SI* makes the largest positive contribution to seasonal *RF* variability both on regional and global scales, followed by the negative contribution of *LAPs*. Our findings augment those of previous comparative analysis, confirming that *SI* plays a leading role, whereas the impact of *SZA* is minor, further demonstrating the viability of the quantitative attribution method.

### 3.4. Interannual RF Variance and Attribution

In this study, the MODIS satellite data are utilised to investigate interannual *RF* variations in the northern hemisphere between 2003 and 2018. As shown in Figure 7g, although *RF* fluctuates between 3.2 and 3.6 W m$^{-2}$, it does not exhibit a clear trend over the last 16 years. Similar characteristics also occur in GRL, HNA, MEUA, and MNA, where trends are weak and statistically insignificant. However, for both HEUA and NEC, *RF* exhibits a significant decrease (at 99% and 98% confidence, respectively) over the period 2003–2018, declining from 4.3 to 3.5 W m$^{-2}$ in HEUA and from 12.3 to 11.3 W m$^{-2}$ in NEC, with corresponding average rates of $-0.04$ and $-0.14$ W m$^{-2}$ a$^{-1}$, respectively. Employing the sensitivity test, we sought to establish the primary factor controlling the observed decline in *RF*.

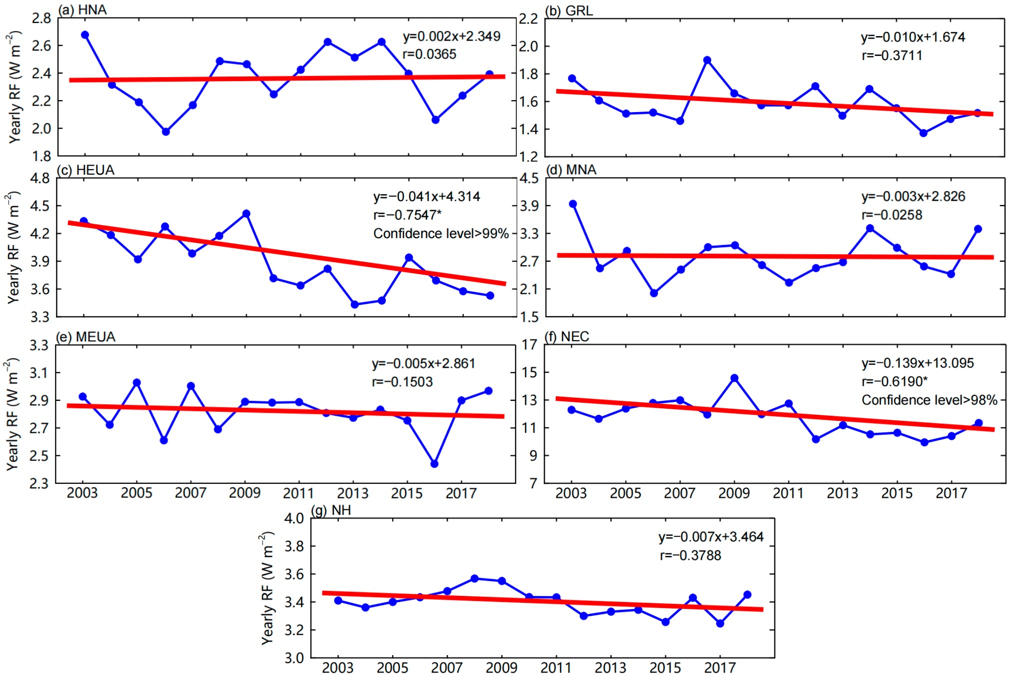

**Figure 7.** Yearly radiative forcing variations in (**a**) HNA, (**b**) GRL, (**c**) HEUA, (**d**) MNA, (**e**) MEUA, (**f**) NEC, and (**g**) the NH. The trend values passing the 95% confidence level are marked by asterisks (*).

As depicted in Figure 8, *LAPs* play the predominant role in the long-term pattern of declining *RF* in HEUA and NEC. Specifically, *LAPs* account for −0.024 W m$^{-2}$ a$^{-1}$ of the HEUA decline and −0.068 W m$^{-2}$ a$^{-1}$ of the NEC decline, thereby accounting for around 50% of the total 2003–2018 decrease in both regions. Our sensitivity test results also indicate that the LAP-induced decreases in both regions are significant at the 98% (HEUA) and 99% (NEC) confidence levels (Figures S9 and S10). After *LAPs*, *SI* is the second most important factor influencing declining *RF*, both in NEC and HEUA, although we note that the SI-induced decrease is statistically insignificant. *SWE* contributes moderately to NEC, whereas the relative impacts of *CF*, *SGS*, and *SZA* are negligible.

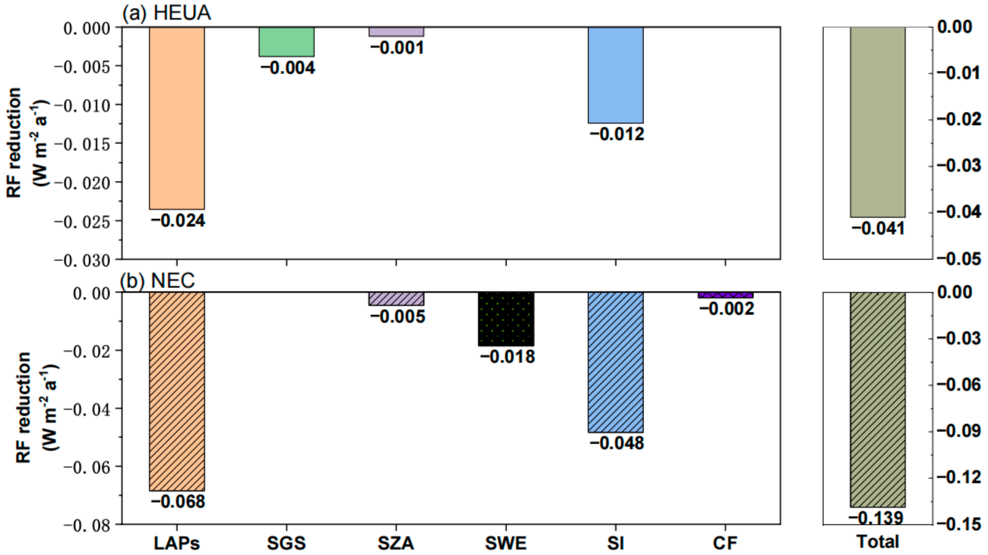

**Figure 8.** Specific values for *LAPs*, *SGS*, *SZA*, *SWE*, *SI*, and *CF*, along with the cumulative decrease in annual radiative forcing in (**a**) HEUA and (**b**) NEC.

## 4. Discussion

Our retrieved *RF* values align with those of Dang et al. (2017) [19], who indicated January–February *RF* from NEC (~7–18 W m$^{-2}$ in 2010) that are comparable to both our 16-year mean (~4.3–19.0 W m$^{-2}$) and the values reported by Zhao et al. (2014) [40] for the same period (10 W m$^{-2}$). However, while Qian et al. (2014) [25] reported significant *RF* values (5–10 W m$^{-2}$) from NEC in April, we note that this region is essentially snow-free by that time and suggest that satellite observations are more effective than the model simulations at constraining snowpack extent. Consequently, modelling studies might overestimate *RF* values in certain mid-latitude regions, such as NEC, owing to inaccurate definition of the springtime snow-covered area.

As detailed information is lacking for MEUA as a whole, we compare our retrievals with the previous in situ study of northwestern China by Shi et al. (2019) [85], who reported January (2018) *RF* values of 0.2–6.9 W m$^{-2}$; the multi-year average in our study is 2.7 W m$^{-2}$. In MNA, Qian et al. (2009) [80] and Oaida et al. (2015) [86] provided simulated March and spring values of 3–7 and 16 W m$^{-2}$, respectively, which aligns well with our retrievals (4.6 W m$^{-2}$) for the same periods. Although these results have confirmed the viability of monthly mid-latitude retrievals, previous work at high latitudes has typically returned springtime *RF* values that are lower (<1 W m$^{-2}$) than those calculated by our study, suggesting that retrieval uncertainties are larger at high latitudes than at middle latitudes.

Previous studies indicated that snow grain shape and LAPs-snow mixing state can also be important in determining *RF* [57,87–89]. They pointed out that snow nonsphericity could reduce the forward scattering and then increase albedo compared with the spherical counterparts. On the other hand, BC-snow internal mixing remarkably reduced albedo compared with external mixing due to an enhancement to snow single-scattering co-albedo [90–92]. A recent work simulated *RF* by considering different snow grain shapes and mixing states of LAPs-snow, then compared it with two satellite-based snow products retrieved from MODIS [93]. The results demonstrated that the comprehensive influence may be negative or positive because of complex and non-linear interactions from these factors. However, we note that we just use a retrieval method for calculations in this study, which is reversed to the above studies. That means the snow grain shape assumption has little influence in pure snow albedo retrieval through the method in Section 2.5.3 [19,94] while the dirty snow albedo in this study is directly derived from the observed MODIS product according to Equation (6). So, the albedo reduction and *RF* calculated according to the retrieved pure and dirty snow albedos (Equations (7) and (8)) are little influenced by the assumption of snow grain shape and the mixing state of LAPs-snow. Therefore, we just use the default assumption (i.e., *LAPs* (equivalent BC) external mixed with spherical snow grains) in the SNICAR model.

Our results imply that shifting air pollution levels over the last 16 years have played a key role in *RF* variability over both regions. In support of this scenario, Figure 9 presents the interannual variations of light-absorbing aerosol concentrations collected from in situ measurements made in HEUA and NEC [62,95–98]. In the former, Panchenko et al. (2021) [95] observed a decrease of 1.5% a$^{-1}$ between 1997 and 2018 in the Tomsk region of Southwestern Siberia (central HEUA). Similarly, Dutkiewicz et al. (2014) [97] reported that BC concentrations at Kevo, Finland (western HEUA) declined by ~1.8% a$^{-1}$ during all seasons between 1970 and 2010, with a total reduction of ~100 ng m$^{-3}$ between 2001 and 2010. Elsewhere in HEUA, BC concentrations declined by 5% a$^{-1}$ in Zeppelin (Ny-Ålesund) between 2007 and 2017 and by 11% a$^{-1}$ in Tiksi (northeastern HEUA) between 2010 and 2018 [62].

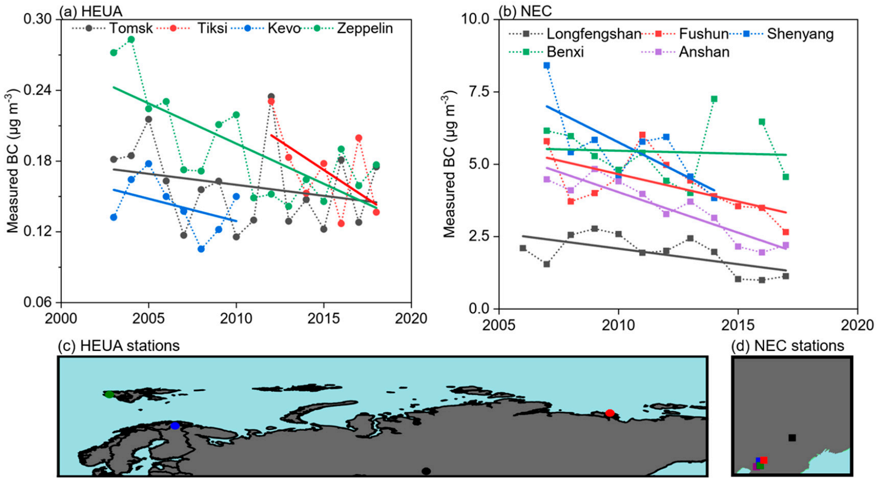

**Figure 9.** Measured BC concentrations at ground-based stations in (**a**) HEUA and (**b**) NEC. In HEUA, the green dot represents Zeppelin, the blue dot Kevo, the black dot Tomsk, and the red dot Tiksi. In NEC, the purple diamond represents Anshan, the green diamond Benxi, the blue diamond Shenyang, the red diamond Fushun, and the black diamond Longfengshan. Spatial distribution of in-situ sites in HEUA and NEC are shown in (**c**) and (**d**), respectively.

Meanwhile, in NEC, Guo et al. (2020) [98] observed declining BC concentrations between 2006 and 2017, with the most significant shifts in urban areas such as Shenyang and Anshan. Together, these observational data suggested that the measured reduction in *RF* in both HEUA and NEC was driven by decreasing air pollution, thus confirming the importance of emissions mitigation for regional and global radiative balances.

In addition, the observed decrease in Eurasian concentrations of light-absorbing substances over the past 20 years is robust, and the corresponding pattern of radiative forcing throughout the snow-covered area of the northern hemisphere exhibits considerable regional variability. In certain regions, trends are weak and/or statistically insignificant. Recognising that the 16-year duration of our study may be insufficient to capture climatology fully, establishing the exact causes of declining northern hemisphere radiative forcing will require further modelling and verification. Similarly, whether the observed changes in pollution emissions, transport, and deposition are driven by anthropogenic or natural processes remains an open question, as does the radiative impact of *LAPs* on climatic and hydrologic change. Ultimately, these and other knowledge gaps will be best addressed by prioritising greater spatial coverage of in situ observations, collection of higher-resolution and longer remote sensing datasets, and more advanced model simulations.

## 5. Conclusions

In this study, we use remote sensing to evaluate northern hemisphere snowpack *RF* (December–May) between 2003 and 2018 over the snow-covered period. The extent of the ISCA varies from month to month, reflecting the progression of winter into spring, and radiative forcing values rise accordingly. To be specific, the spatial patterns of *RF*, where primarily located in mid-latitude regions, are similar between December and January. Furthermore, the *RF* at high latitudes could be retrieved after March when the polar night duration ends. *RF* peak in March due to the snow ablation in most mid-latitudes but would continue to increase in high latitudes resulting from the higher daily solar irradiance. Following our assessment of the spatial distribution and temporal variability of *RF*, we make quantitative attributions of spatial and temporal variability to radiative forcing. We observe that *SWE* is the dominant contributor to spatial variability in wintertime mid-latitude radiative forcing, whereas LAP contributes most to high-latitude *RF* in spring. In contrast, *SI* plays a more important role in the spatial *RF* variability at high latitudes, with this contribution decreasing almost monotonously over time as the LAP contribution rises. *SGS* accounts for only ~10% of the spatial variance in GRL, reflecting the gradient distribution between coastal and inland regions during our study period. We also find that *SZA* only becomes important when high values are attained over a broad latitudinal range. On both regional and global scales, *SI* is the greatest contributor to temporal radiative forcing variability, followed by LAPs; the impact of *SWE* is non-negligible at mid-latitudes, where the snowpack is relatively heterogeneous. Finally, the decreasing trends in radiative forcing over HEUA ($-0.04$ W m$^{-2}$ a$^{-1}$) and NEC ($-0.14$ W m$^{-2}$ a$^{-1}$) between 2003 and 2018 are significant at 98% and 99% confidence levels, respectively. The concentration of *LAPs* dominates this pattern, resulting in radiative forcing variations of $-0.024$ W m$^{-2}$ a$^{-1}$ in HEUA and $-0.068$ W m$^{-2}$ a$^{-1}$ in NEC, followed by the *SI*, which accounts for $-0.012$ W m$^{-2}$ a$^{-1}$ (HEUA) and $-0.048$ W m $^{-2}$ a$^{-1}$ (NEC) of interannual variability. These results confirm that levels of airborne pollution decreased during the observation period in both HEUA and NEC, thereby supporting the findings of previous studies [40,68–71].

**Supplementary Materials:** The following supporting information can be downloaded at: https://www.mdpi.com/article/10.3390/rs15030636/s1, Figure S1: Land cover types; Figure S2: Spatial distributions of averaged multi-year (2003–2018) $I_{imp}$; Figure S3: Spatial distributions of averaged multi-year (2003–2018) *SGS*; Figure S4: Spatial distributions of averaged multi-year (2003–2018) *SZA*; Figure S5: Spatial distributions of averaged multi-year (2003–2018) *SWE*; Figure S6: Spatial distributions of averaged multi-year (2003–2018) *SI*; Figure S7: Spatial distributions of averaged multi-year (2003–2018) *SI*; Figure S8: Monthly radiative forcing for each region during the period 2003–2018; Figure S9: *RF* variations in HUEA due to each forcing factor; Figure S10: *RF* variations in NEC due to each forcing factor.

**Author Contributions:** Conceptualization, J.C. and W.P.; Data curation, J.C.; Formal analysis, X.W.; Funding acquisition, X.W. and W.P.; Investigation, J.C. and W.P.; Methodology, X.N., Y.X. and S.Y.; Project administration, X.W.; Resources, J.Z. and L.C.; Software, Y.C.; Supervision, W.P.; Visualization, J.C.; Writing—original draft, J.C., S.X. and D.W.; Writing—review and editing, T.S. All authors have read and agreed to the published version of the manuscript.

**Funding:** This research was supported by the National Natural Science Foundation of China (42075061), the National Science Fund for Distinguished Young Scholars (42025102), and the National Natural Science Foundation of China (41975157).

**Data Availability Statement:** MODIS data can be found at https://earthdata.nasa.gov (accessed on 15 October 2022). CERES data can be found from NASA's Clouds and the Earth's Radiant Energy System at https://ceres.larc.nasa.gov (accessed on 15 October 2022). *SWE* data can be found from ERA5 at https://www.ecmwf.int (accessed on 15 October 2022).

**Acknowledgments:** We thank Lanzhou City's scientific research funding subsidy to Lanzhou University and the Supercomputing Center of Lanzhou University for providing the computing services.

**Conflicts of Interest:** The authors declare no conflict of interest.

## Abbreviations

| ACRONYM | Definition |
|---|---|
| BC | Black carbon |
| BHR | Bi-hemispherical reflectance |
| BRDF | Bidirectional Reflectance Distribution Function |
| CAM5 | Community Atmosphere Model version 5 |
| CERES | Clouds and the Earth's Radiant Energy System |
| CF | Cloud fraction |
| DHR | Directional hemispherical reflectance |
| ECMWF | European Centre for Medium-Range Weather Forecasts |
| FSC | Fractional Snow Cover |
| GRL | Greenland |
| HEUA | High-latitude Eurasia |
| HNA | High-latitude North America |

| | |
|---|---|
| IMS | Interactive Multisensor Snow and Ice Mapping System |
| ISCA | Identified snow-covered area |
| LAPS | Light-absorbing particles |
| MEUA | Mid-latitude Eurasia |
| MNA | Mid-latitude North America |
| MODIS | Moderate Resolution Imaging Spectroradiometer |
| NDSI | Normalized Difference Snow Index |
| NEC | Northeastern China |
| NIR | Near-infrared |
| OC | Organic carbon |
| OLI | Operational Land Imager |
| RF | Radiative forcing |
| SBDART | The Santa Barbara DISORT Atmospheric Radiative Transfer |
| SGS | Snow grain sizes |
| SI | Solar irradiance |
| SNICAR | Snow, Ice, and Aerosol Radiative model |
| SNOWPACK | Multilayer, physically based snow-process model |
| SRTM | Shuttle Radar Topography Mission |
| SWE | Snow water equivalent |
| SZA | Solar zenith angle |
| UAV | Unmanned Aerial Vehicle |

## References

1. Betts, A.K.; Ball, J.H. Albedo over the boreal forest. *J. Geophys. Res. Atmos.* **1997**, *102*, 28901–28909. [CrossRef]
2. Picard, G.; Dumont, M.; Lamare, M.; Tuzet, F.; Larue, F.; Pirazzini, R.; Arnaud, L. Spectral albedo measurements over snow-covered slopes: Theory and slope effect corrections. *Cryosphere* **2020**, *14*, 1497–1517. [CrossRef]
3. Painter, T.H.; Roberts, D.A.; Green, R.O.; Dozier, J. The Effect of Grain Size on Spectral Mixture Analysis of Snow-Covered Area from AVIRIS Data. *Remote Sens. Environ.* **1998**, *65*, 320–332. [CrossRef]
4. Warren, S.G. Optical properties of snow. *Rev. Geophys.* **1982**, *20*, 67. [CrossRef]
5. Warren, S.G. Impurities in Snow: Effects on Albedo and Snowmelt (Review). *Ann. Glaciol.* **1984**, *5*, 177–179. [CrossRef]
6. Mu, Z.; Niu, X.; George, C.; Wang, X.; Huang, R.; Ma, Y.; Pu, W.; Qi, Y.; Fu, P.; Deng, J.; et al. Accumulation of dissolved organic matter in the transition from fresh to aged seasonal snow in an industrial city in NE China. *Sci. Total Environ.* **2023**, *857*, 159337. [CrossRef]
7. Niu, X.; Pu, W.; Fu, P.; Chen, Y.; Xing, Y.; Wu, D.; Chen, Z.; Shi, T.; Zhou, Y.; Wen, H.; et al. Fluorescence characteristics, absorption properties, and radiative effects of water-soluble organic carbon in seasonal snow across northeastern China. *Atmos. Chem. Phys.* **2022**, *22*, 14075–14094. [CrossRef]
8. Zhou, Y.; Wen, H.; Liu, J.; Pu, W.; Chen, Q.; Wang, X. The optical characteristics and sources of chromophoric dissolved organic matter (CDOM) in seasonal snow of northwestern China. *Cryosphere* **2019**, *13*, 157–175. [CrossRef]
9. Zhou, Y.; West, C.P.; Hettiyadura, A.P.S.; Niu, X.; Wen, H.; Cui, J.; Shi, T.; Pu, W.; Wang, X.; Laskin, A. Measurement report: Molecular composition, optical properties, and radiative effects of water-soluble organic carbon in snowpack samples from northern Xinjiang, China. *Atmos. Chem. Phys.* **2021**, *21*, 8531–8555. [CrossRef]
10. Painter, T.H.; Skiles, S.M.; Deems, J.S.; Bryant, A.C.; Landry, C.C. Dust radiative forcing in snow of the Upper Colorado River Basin: 1. A 6 year record of energy balance, radiation, and dust concentrations. *Water Resour. Res.* **2012**, *48*, W07521. [CrossRef]
11. Warren, S.G.; Brandt, R.E. Optical constants of ice from the ultraviolet to the microwave: A revised compilation. *J. Geophys. Res.* **2008**, *113*, D14220. [CrossRef]
12. Shi, T.; Chen, Y.; Xing, Y.; Niu, X.; Wu, D.; Cui, J.; Zhou, Y.; Pu, W.; Wang, X. Assessment of the combined radiative effects of black carbon in the atmosphere and snowpack in the Northern Hemisphere constrained by surface observations. *Environ. Sci. Atmos.* **2022**, *2*, 702–713. [CrossRef]
13. Wang, X.; Shi, T.; Zhang, X.; Chen, Y. An Overview of Snow Albedo Sensitivity to Black Carbon Contamination and Snow Grain Properties Based on Experimental Datasets Across the Northern Hemisphere. *Curr. Pollut. Rep.* **2020**, *6*, 368–379. [CrossRef]
14. Cui, J.; Shi, T.; Zhou, Y.; Wu, D.; Wang, X.; Pu, W. Satellite-based radiative forcing by light-absorbing particles in snow across the Northern Hemisphere. *Atmos. Chem. Phys.* **2021**, *21*, 269–288. [CrossRef]
15. Wielicki, B.A.; Wong, T.; Loeb, N.; Minnis, P.; Priestley, K.; Kandel, R. Changes in Earth's albedo measured by satellite. *Science* **2005**, *308*, 825. [CrossRef]
16. Wang, X.; Pu, W.; Zhang, X.; Ren, Y.; Huang, J. Water-soluble ions and trace elements in surface snow and their potential source regions across northeastern China. *Atmos. Environ.* **2015**, *114*, 57–65. [CrossRef]
17. Wang, X.; Xu, B.; Ming, J. An overview of the studies on black carbon and mineral dust deposition in snow and ice cores in East Asia. *J. Meteorol. Res.* **2014**, *28*, 354–370. [CrossRef]

18. Wang, X.; Pu, W.; Shi, J.; Bi, J.; Zhou, T.; Zhang, X.; Ren, Y. A comparison of the physical and optical properties of anthropogenic air pollutants and mineral dust over Northwest China. *J. Meteorol. Res.* **2015**, *29*, 180–200. [CrossRef]
19. Dang, C.; Warren, S.G.; Fu, Q.; Doherty, S.J.; Sturm, M.; Su, J. Measurements of light-absorbing particles in snow across the Arctic, North America, and China: Effects on surface albedo. *J. Geophys. Res.* **2017**, *122*, 10149–10168. [CrossRef]
20. Ganey, G.Q.; Loso, M.G.; Burgess, A.B.; Dial, R.J. The role of microbes in snowmelt and radiative forcing on an Alaskan icefield. *Nat. Geosci.* **2017**, *10*, 754–759. [CrossRef]
21. Skiles, S.M.; Painter, T.H.; Deems, J.S.; Bryant, A.C.; Landry, C.C. Dust radiative forcing in snow of the Upper Colorado River Basin: 2. Interannual variability in radiative forcing and snowmelt rates. *Water Resour. Res.* **2012**, *48*, W07522. [CrossRef]
22. Pu, W.; Wang, X.; Wei, H.; Zhou, Y.; Shi, J.; Hu, Z.; Jin, H.; Chen, Q. Properties of black carbon and other insoluble light-absorbing particles in seasonal snow of northwestern China. *Cryosphere* **2017**, *11*, 1213–1233. [CrossRef]
23. Wang, X.; Wei, H.; Liu, J.; Xu, B.; Wang, M.; Ji, M.; Jin, H. Quantifying the light absorption and source attribution of insoluble light-absorbing particles on Tibetan Plateau glaciers between 2013 and 2015. *Cryosphere* **2019**, *13*, 309–324. [CrossRef]
24. Wang, X.; Zhang, X.; Di, W. Development of an improved two-sphere integration technique for quantifying black carbon concentrations in the atmosphere and seasonal snow. *Atmos. Meas. Tech.* **2020**, *13*, 39–52. [CrossRef]
25. Qian, Y.; Wang, H.; Zhang, R.; Flanner, M.G.; Rasch, P.J. A sensitivity study on modeling black carbon in snow and its radiative forcing over the Arctic and Northern China. *Environ. Res. Lett.* **2014**, *9*, 064001. [CrossRef]
26. Young, C.L.; Sokolik, I.N.; Flanner, M.G.; Dufek, J. Surface radiative impacts of ash deposits from the 2009 eruption of Redoubt volcano. *J. Geophys. Res. Atmos.* **2014**, *119*, 11,387–11,397. [CrossRef]
27. Skiles, S.M.; Painter, T.H. Toward Understanding Direct Absorption and Grain Size Feedbacks by Dust Radiative Forcing in Snow with Coupled Snow Physical and Radiative Transfer Modeling. *Water Resour. Res.* **2019**, *55*, 7362–7378. [CrossRef]
28. Skiles, S.M.; Mallia, D.V.; Hallar, A.G.; Lin, J.C.; Lambert, A.; Petersen, R.; Clark, S. Implications of a shrinking Great Salt Lake for dust on snow deposition in the Wasatch Mountains, UT, as informed by a source to sink case study from the 13–14 April 2017 dust event. *Environ. Res. Lett.* **2018**, *13*, 124031. [CrossRef]
29. Pu, W.; Cui, J.; Wu, D.; Shi, T.; Chen, Y.; Xing, Y.; Zhou, Y.; Wang, X. Unprecedented snow darkening and melting in New Zealand due to 2019–2020 Australian wildfires. *Fundam. Res.* **2021**, *1*, 224–231. [CrossRef]
30. Bryant, A.C.; Painter, T.H.; Deems, J.S.; Bender, S.M. Impact of dust radiative forcing in snow on accuracy of operational runoff prediction in the Upper Colorado River Basin. *Geophys. Res. Lett.* **2013**, *40*, 3945–3949. [CrossRef]
31. Di Mauro, B.; Fava, F.; Ferrero, L.; Garzonio, R.; Baccolo, G.; Delmonte, B.; Colombo, R. Mineral dust impact on snow radiative properties in the European Alps combining ground, UAV, and satellite observations. *J. Geophys. Res. Atmos.* **2015**, *120*, 6080–6097. [CrossRef]
32. Chen, W.; Wang, X.; Cui, J.; Cao, X.; Pu, W.; Zheng, X.; Ran, H.; Ding, J. Radiative forcing of black carbon in seasonal snow of wintertime based on remote sensing over Xinjiang, China. *Atmos. Environ.* **2021**, *247*, 118204. [CrossRef]
33. Skiles, S.M.; Flanner, M.; Cook, J.M.; Dumont, M.; Painter, T.H. Radiative forcing by light-absorbing particles in snow. *Nat. Clim. Chang.* **2018**, *8*, 964–971. [CrossRef]
34. Bond, T.C.; Doherty, S.J.; Fahey, D.W.; Forster, P.M.; Berntsen, T.; DeAngelo, B.J.; Flanner, M.G.; Ghan, S.; Kärcher, B.; Koch, D.; et al. Bounding the role of black carbon in the climate system: A scientific assessment. *J. Geophys. Res. Atmos.* **2013**, *118*, 5380–5552. [CrossRef]
35. Kaspari, S.; Painter, T.H.; Gysel, M.; Skiles, S.M.; Schwikowski, M. Seasonal and elevational variations of black carbon and dust in snow and ice in the Solu-Khumbu, Nepal and estimated radiative forcings. *Atmos. Chem. Phys.* **2014**, *14*, 8089–8103. [CrossRef]
36. Skiles, S.M.; Painter, T. Daily evolution in dust and black carbon content, snow grain size, and snow albedo during snowmelt, Rocky Mountains, Colorado. *J. Glaciol.* **2016**, *63*, 118–132. [CrossRef]
37. Zhou, Y.; West, C.P.; Hettiyadura, A.P.S.; Pu, W.; Shi, T.; Niu, X.; Wen, H.; Cui, J.; Wang, X.; Laskin, A. Molecular Characterization of Water-Soluble Brown Carbon Chromophores in Snowpack from Northern Xinjiang, China. *Env. Sci. Technol.* **2022**, *56*, 4173–4186. [CrossRef]
38. Xu, B.; Cao, J.; Hansen, J.; Yao, T.; Joswia, D.R.; Wang, N.; Wu, G.; Wang, M.; Zhao, H.; Yang, W.; et al. Black soot and the survival of Tibetan glaciers. *Proc. Natl. Acad. Sci. USA* **2009**, *106*, 22114–22118. [CrossRef]
39. Kang, S.; Zhang, Q.; Zhang, Y.; Guo, W.; Ji, Z.; Shen, M.; Wang, S.; Wang, X.; Tripathee, L.; Liu, Y.; et al. Warming and thawing in the Mt. Everest region: A review of climate and environmental changes. *Earth-Sci. Rev.* **2022**, *225*, 103911. [CrossRef]
40. Zhao, C.; Hu, Z.; Qian, Y.; Ruby Leung, L.; Huang, J.; Huang, M.; Jin, J.; Flanner, M.G.; Zhang, R.; Wang, H.; et al. Simulating black carbon and dust and their radiative forcing in seasonal snow: A case study over North China with field campaign measurements. *Atmos. Chem. Phys.* **2014**, *14*, 11475–11491. [CrossRef]
41. Qi, L.; Li, Q.; Li, Y.; He, C. Factors controlling black carbon distribution in the Arctic. *Atmos. Chem. Phys.* **2017**, *17*, 1037–1059. [CrossRef]
42. Schaaf, C.B.; Gao, F.; Strahler, A.H.; Lucht, W.; Li, X.W.; Tsang, T.; Strugnell, N.C.; Zhang, X.Y.; Jin, Y.F.; Muller, J.P.; et al. First operational BRDF, albedo nadir reflectance products from MODIS. *Remote Sens. Environ.* **2002**, *83*, 135–148. [CrossRef]
43. Schaaf, C.B.; Wang, Z.; Strahler, A.H. Commentary on Wang and Zender—MODIS snow albedo bias at high solar zenith angles relative to theory and to in situ observations in Greenland. *Remote. Sens. Environ.* **2011**, *115*, 1296–1300. [CrossRef]
44. Wang, Z.; Schaaf, C.B.; Sun, Q.; Shuai, Y.; Román, M.O. Capturing rapid land surface dynamics with Collection V006 MODIS BRDF/NBAR/Albedo (MCD43) products. *Remote. Sens. Environ.* **2018**, *207*, 50–64. [CrossRef]

45. Jin, Y.; Schaaf, C.B.; Gao, F.; Li, X.; Strahler, A.H.; Lucht, W.; Liang, S. Consistency of MODIS surface bidirectional reflectance distribution function and albedo retrievals: 1. Algorithm performance. *J. Geophys. Res.* **2003**, *108*, 4158. [CrossRef]
46. Jin, Y.; Schaaf, C.B.; Woodcock, C.E.; Gao, F.; Li, X.; Strahler, A.H.; Lucht, W.; Liang, S. Consistency of MODIS surface bidirectional reflectance distribution function and albedo retrievals: 2. Validation. *J. Geophys. Res.* **2003**, *108*, 4159. [CrossRef]
47. Liu, J.; Schaaf, C.; Strahler, A.; Jiao, Z.; Shuai, Y.; Zhang, Q.; Roman, M.; Augustine, J.A.; Dutton, E.G. Validation of Moderate Resolution Imaging Spectroradiometer (MODIS) albedo retrieval algorithm: Dependence of albedo on solar zenith angle. *J. Geophys. Res. Atmos.* **2009**, *114*, D01106. [CrossRef]
48. Loeb, N.G.; Doelling, D.R.; Keyes, D.F.; Nordeen, M.L.; Morstad, D.; Nguyen, C.; Wielicki, B.A.; Young, D.F.; Sun, M. Geostationary Enhanced Temporal Interpolation for CERES Flux Products. *J. Atmos. Ocean. Technol.* **2013**, *30*, 1072–1090. [CrossRef]
49. Hersbach, H.; Bell, B.; Berrisford, P.; Hirahara, S.; Horányi, A.; Muñoz-Sabater, J.; Nicolas, J.; Peubey, C.; Radu, R.; Schepers, D. The ERA5 global reanalysis. *QJ Roy. Meteor. Soc.* **2020**, *146*, 1999–2049. [CrossRef]
50. Dutra, E.; Balsamo, G.; Viterbo, P.; Miranda, P.M.A.; Beljaars, A.; Schär, C.; Elder, K. An Improved Snow Scheme for the ECMWF Land Surface Model: Description and Offline Validation. *J. Hydrometeorol.* **2010**, *11*, 899–916. [CrossRef]
51. Nogueira, M. Inter-comparison of ERA-5, ERA-interim and GPCP rainfall over the last 40 years: Process-based analysis of systematic and random differences. *J. Hydrol.* **2020**, *583*, 124632. [CrossRef]
52. Ou, T.; Chen, D.; Chen, X.; Lin, C.; Yang, K.; Lai, H.-W.; Zhang, F. Simulation of summer precipitation diurnal cycles over the Tibetan Plateau at the gray-zone grid spacing for cumulus parameterization. *Clim. Dyn.* **2020**, *54*, 3525–3539. [CrossRef]
53. Cao, B.; Gruber, S.; Zheng, D.; Li, X. The ERA5-Land soil temperature bias in permafrost regions. *Cryosphere* **2020**, *14*, 2581–2595. [CrossRef]
54. de Rosnay, P.; Balsamo, G.; Albergel, C.; Muñoz-Sabater, J.; Isaksen, L. Initialisation of Land Surface Variables for Numerical Weather Prediction. *Surv. Geophys.* **2012**, *35*, 607–621. [CrossRef]
55. Toon, O.B.; McKay, C.P.; Ackerman, T.P.; Santhanam, K. Rapid calculation of radiative heating rates and photodissociation rates in inhomogeneous multiple scattering atmospheres. *J. Geophys. Res.* **1989**, *94*, 16287. [CrossRef]
56. Flanner, M.G.; Zender, C.S.; Randerson, J.T.; Rasch, P.J. Present-day climate forcing and response from black carbon in snow. *J. Geophys. Res.* **2007**, *112*, D11202. [CrossRef]
57. He, C.; Flanner, M.G.; Chen, F.; Barlage, M.; Liou, K.-N.; Kang, S.; Ming, J.; Qian, Y. Black carbon-induced snow albedo reduction over the Tibetan Plateau: Uncertainties from snow grain shape and aerosol–snow mixing state based on an updated SNICAR model. *Atmos. Chem. Phys.* **2018**, *18*, 11507–11527. [CrossRef]
58. Pu, W.; Cui, J.; Shi, T.; Zhang, X.; He, C.; Wang, X. The remote sensing of radiative forcing by light-absorbing particles (LAPs) in seasonal snow over northeastern China. *Atmos. Chem. Phys.* **2019**, *19*, 9949–9968. [CrossRef]
59. Dang, C.; Zender, C.S.; Flanner, M.G. Intercomparison and improvement of two-stream shortwave radiative transfer schemes in Earth system models for a unified treatment of cryospheric surfaces. *Cryosphere* **2019**, *13*, 2325–2343. [CrossRef]
60. Briegleb, B.; Light, B. A Delta-Eddington mutiple scattering parameterization for solar radiation in the sea ice component of the community climate system model. In *NCAR Technical Note*; NCAR: Boulder, CO, USA, 2007. [CrossRef]
61. Flanner, M.G.; Arnheim, J.B.; Cook, J.M.; Dang, C.; He, C.; Huang, X.; Singh, D.; Skiles, S.M.; Whicker, C.A.; Zender, C.S. SNICAR-ADv3: A community tool for modeling spectral snow albedo. *Geosci. Model Dev.* **2021**, *14*, 7673–7704. [CrossRef]
62. Schmale, J.; Sharma, S.; Decesari, S.; Pernov, J.; Massling, A.; Hansson, H.-C.; von Salzen, K.; Skov, H.; Andrews, E.; Quinn, P.K.; et al. Pan-Arctic seasonal cycles and long-term trends of aerosol properties from 10 observatories. *Atmos. Chem. Phys.* **2022**, *22*, 3067–3096. [CrossRef]
63. Negi, H.S.; Kokhanovsky, A. Retrieval of snow grain size and albedo of western Himalayan snow cover using satellite data. *Cryosphere* **2011**, *5*, 831–847. [CrossRef]
64. Lewis, P.; Barnsley, M. Influence of the sky radiance distribution on various formulations of the earth surface albedo. In Proceedings of the 6th International Symposium on Physical Measurements and Signatures in Remote Sensing, ISPRS, Val D'Isere, France, 17–21 January 1994; pp. 707–715.
65. Siegmund, A.M.; Gunter. Fernes nah gebracht-Satelliten- und Luftbildeinsatz zur Analyse von Umweltveränderungen im Geographieunterricht. *Geogr. Und Sch.* **2005**, *27*, 2–10.
66. Nolin, A.W.; Dozier, J. A Hyperspectral Method for Remotely Sensing the Grain Size of Snow. *Remote Sens. Environ.* **2000**, *74*, 207–216. [CrossRef]
67. Painter, T.H.; Seidel, F.C.; Bryant, A.C.; McKenzie Skiles, S.; Rittger, K. Imaging spectroscopy of albedo and radiative forcing by light-absorbing impurities in mountain snow. *J. Geophys. Res. Atmos.* **2013**, *118*, 9511–9523. [CrossRef]
68. Seidel, F.C.; Rittger, K.; Skiles, S.M.; Molotch, N.P.; Painter, T.H. Case study of spatial and temporal variability of snow cover, grain size, albedo and radiative forcing in the Sierra Nevada and Rocky Mountain snowpack derived from imaging spectroscopy. *Cryosphere* **2016**, *10*, 1229–1244. [CrossRef]
69. Painter, T.H.; Rittger, K.; McKenzie, C.; Slaughter, P.; Davis, R.E.; Dozier, J. Retrieval of subpixel snow covered area, grain size, and albedo from MODIS. *Remote Sens. Environ.* **2009**, *113*, 868–879. [CrossRef]
70. Wu, D.; Liu, J.; Wang, T.; Niu, X.; Chen, Z.; Wang, D.; Zhang, X.; Ji, M.; Wang, X.; Pu, W. Applying a dust index over North China and evaluating the contribution of potential factors to its distribution. *Atmos. Res.* **2021**, *254*, 105515. [CrossRef]

71. Jin, X.; Li, Z.; Wu, T.; Wang, Y.; Su, T.; Ren, R.; Wu, H.; Zhang, D.; Li, S.; Cribb, M. Differentiating the Contributions of Particle Concentration, Humidity, and Hygroscopicity to Aerosol Light Scattering at Three Sites in China. *J. Geophys. Res. Atmos.* **2022**, *127*, e2022JD036891. [CrossRef]
72. Huang, J.; Yi, Y. Inversion of a nonlinear dynamical model from the observation. *Sci. China Ser.B* **1991**, *10*, 1246–1251.
73. Räisänen, P.; Makkonen, R.; Kirkevåg, A.; Debernard, J.B. Effects of snow grain shape on climate simulations: Sensitivity tests with the Norwegian Earth System Model. *Cryosphere* **2017**, *11*, 2919–2942. [CrossRef]
74. Doherty, S.J.; Warren, S.G.; Grenfell, T.C.; Clarke, A.D.; Brandt, R.E. Light-absorbing impurities in Arctic snow. *Atmos. Chem. Phys.* **2010**, *10*, 11647–11680. [CrossRef]
75. Doherty, S.J.; Grenfell, T.C.; Forsström, S.; Hegg, D.L.; Brandt, R.E.; Warren, S.G. Observed vertical redistribution of black carbon and other insoluble light-absorbing particles in melting snow. *J. Geophys. Res. Atmos.* **2013**, *118*, 5553–5569. [CrossRef]
76. Ye, H.; Zhang, R.; Shi, J.; Huang, J.; Warren, S.G.; Fu, Q. Black carbon in seasonal snow across northern Xinjiang in northwestern China. *Environ. Res. Lett.* **2012**, *7*, 044002. [CrossRef]
77. Wang, X.; Doherty, S.J.; Huang, J. Black carbon and other light-absorbing impurities in snow across Northern China. *J. Geophys. Res. Atmos.* **2013**, *118*, 1471–1492. [CrossRef]
78. Wang, X.; Pu, W.; Ren, Y.; Zhang, X.; Zhang, X.; Shi, J.; Jin, H.; Dai, M.; Chen, Q. Observations and model simulations of snow albedo reduction in seasonal snow due to insoluble light-absorbing particles during 2014 Chinese survey. *Atmos. Chem. Phys.* **2017**, *17*, 2279–2296. [CrossRef]
79. Flanner, M.G.; Zender, C.S.; Hess, P.G.; Mahowald, N.M.; Painter, T.H.; Ramanathan, V.; Rasch, P.J. Springtime warming and reduced snow cover from carbonaceous particles. *Atmos. Chem. Phys.* **2009**, *9*, 2481–2497. [CrossRef]
80. Qian, Y.; Gustafson, W.I.; Leung, L.R.; Ghan, S.J. Effects of soot-induced snow albedo change on snowpack and hydrological cycle in western United States based on Weather Research and Forecasting chemistry and regional climate simulations. *J. Geophys. Res.* **2009**, *114*, D03108. [CrossRef]
81. Qian, Y.; Yasunari, T.J.; Doherty, S.J.; Flanner, M.G.; Lau, W.K.M.; Ming, J.; Wang, H.; Wang, M.; Warren, S.G.; Zhang, R. Light-absorbing particles in snow and ice: Measurement and modeling of climatic and hydrological impact. *Adv. Atmos. Sci.* **2015**, *32*, 64–91. [CrossRef]
82. Alexander, P.M.; Tedesco, M.; Fettweis, X.; van de Wal, R.S.W.; Smeets, C.J.P.P.; van den Broeke, M.R. Assessing spatio-temporal variability and trends in modelled and measured Greenland Ice Sheet albedo (2000–2013). *Cryosphere* **2014**, *8*, 2293–2312. [CrossRef]
83. Hadley, O.L.; Kirchstetter, T.W. Black-carbon reduction of snow albedo. *Nat. Clim. Chang.* **2012**, *2*, 437–440. [CrossRef]
84. Ming, J.; Du, Z.; Xiao, C.; Xu, X.; Zhang, D. Darkening of the mid-Himalaya glaciers since 2000 and the potential causes. *Environ. Res. Lett.* **2012**, *7*, 014021. [CrossRef]
85. Shi, T.; Pu, W.; Zhou, Y.; Cui, J.; Zhang, D.; Wang, X. Albedo of Black Carbon-Contaminated Snow Across Northwestern China and the Validation with Model Simulation. *J. Geophys. Res. Atmos.* **2019**, *125*, e2019JD032065. [CrossRef]
86. Oaida, C.M.; Xue, Y.; Flanner, M.G.; Skiles, S.M.; De Sales, F.; Painter, T.H. Improving snow albedo processes in WRF/SSiB regional climate model to assess impact of dust and black carbon in snow on surface energy balance and hydrology over western U.S. *J. Geophys. Res. Atmos.* **2015**, *120*, 3228–3248. [CrossRef]
87. Flanner, M.G.; Liu, X.; Zhou, C.; Penner, J.E.; Jiao, C. Enhanced solar energy absorption by internally-mixed black carbon in snow grains. *Atmos. Chem. Phys.* **2012**, *12*, 4699–4721. [CrossRef]
88. Doherty, S.J.; Hegg, D.A.; Johnson, J.E.; Quinn, P.K.; Schwarz, J.P.; Dang, C.; Warren, S.G. Causes of variability in light absorption by particles in snow at sites in Idaho and Utah. *J. Geophys. Res. Atmos.* **2016**, *121*, 4751–4768. [CrossRef]
89. He, C.; Takano, Y.; Liou, K.-N.; Yang, P.; Li, Q.; Chen, F. Impact of Snow Grain Shape and Black Carbon–Snow Internal Mixing on Snow Optical Properties: Parameterizations for Climate Models. *J. Clim.* **2017**, *30*, 10019–10036. [CrossRef]
90. Shi, T.; Cui, J.; Chen, Y.; Zhou, Y.; Pu, W.; Xu, X.; Chen, Q.; Zhang, X.; Wang, X. Enhanced light absorption and reduced snow albedo due to internally mixed mineral dust in grains of snow. *Atmos. Chem. Phys.* **2021**, *21*, 6035–6051. [CrossRef]
91. Shi, T.; Cui, J.; Wu, D.; Xing, Y.; Chen, Y.; Zhou, Y.; Pu, W.; Wang, X. Snow albedo reductions induced by the internal/external mixing of black carbon and mineral dust, and different snow grain shapes across northern China. *Env. Res.* **2022**, *208*, 112670. [CrossRef]
92. Shi, T.; He, C.; Zhang, D.; Zhang, X.; Niu, X.; Xing, Y.; Chen, Y.; Cui, J.; Pu, W.; Wang, X. Opposite Effects of Mineral Dust Nonsphericity and Size on Dust-Induced Snow Albedo Reduction. *Geophys. Res. Lett.* **2022**, *49*, e2022GL099031. [CrossRef]
93. Hao, D.; Bisht, G.; He, C.; Bair, E.; Huang, H.; Dang, C.; Rittger, K.; Gu, Y.; Wang, H.; Qian, Y.; et al. Improving snow albedo modeling in E3SM land model (version 2.0) and assessing its impacts on snow and surface fluxes over the Tibetan Plateau. *Geosci. Model. Dev.* **2023**, *16*, 75–94. [CrossRef]
94. Dang, C.; Fu, Q.; Warren, S.G. Effect of Snow Grain Shape on Snow Albedo. *J. Atmos. Sci.* **2016**, *73*, 3573–3583. [CrossRef]
95. Panchenko, M.; Yausheva, E.; Chernov, D.; Kozlov, V.; Makarov, V.; Popova, S.; Shmargunov, V. Submicron Aerosol and Black Carbon in the Troposphere of Southwestern Siberia (1997–2018). *Atmosphere* **2021**, *12*, 351. [CrossRef]
96. Schmeisser, L.; Backman, J.; Ogren, J.A.; Andrews, E.; Asmi, E.; Starkweather, S.; Uttal, T.; Fiebig, M.; Sharma, S.; Eleftheriadis, K.; et al. Seasonality of aerosol optical properties in the Arctic. *Atmos. Chem. Phys.* **2018**, *18*, 11599–11622. [CrossRef]

97. Dutkiewicz, V.A.; DeJulio, A.M.; Ahmed, T.; Laing, J.; Hopke, P.K.; Skeie, R.B.; Viisanen, Y.; Paatero, J.; Husain, L. Forty-seven years of weekly atmospheric black carbon measurements in the Finnish Arctic: Decrease in black carbon with declining emissions. *J. Geophys. Res. Atmos.* **2014**, *119*, 7667–7683. [CrossRef]
98. Guo, B.; Wang, Y.; Zhang, X.; Che, H.; Ming, J.; Yi, Z. Long-Term Variation of Black Carbon Aerosol in China Based on Revised Aethalometer Monitoring Data. *Atmosphere* **2020**, *11*, 684. [CrossRef]